JEM

Journal of Electron Microscopy **60(Supplement 1)**: S213–S223 (2011)
doi: 10.1093/jmicro/dfr030

60th Anniversary Issue: Physical

New views of materials through aberration-corrected scanning transmission electron microscopy

S. J. Pennycook* and M. Varela

Oak Ridge National Laboratory, Materials Science and Technology Division, Oak Ridge, TN 37830-6071, USA
*To whom correspondence should be addressed. E-mail: pennycooksj@ornl.gov

Abstract The successful correction of third-order and, more recently, fifth-order aberrations has enormously enhanced the capabilities of the scanning transmission electron microscope (STEM), by not only achieving record resolution, but also allowing near 100% efficiency for electron energy loss spectroscopy, and higher currents for two-dimensional spectrum imaging. These advances have meant that the intrinsic advantages of the STEM, incoherent imaging and simultaneous collection of multiple complementary images can now give new insights into many areas of materials physics. Here, we review a number of examples, mostly from the field of complex oxides, and look towards new directions for the future.

Keywords scanning transmission electron microscopy, electron energy loss spectroscopy, aberration correction, *Z*-contrast

Received 7 March 2011, accepted 5 April 2011

Introduction

It is more than 60 years since Scherzer's pioneering studies of the aberrations of electron lenses and how they might be overcome. His classic paper of 1936 proved that spherical aberration is intrinsically positive for round lenses [1], stating that 'the unavoidability of spherical aberration is a technical barrier but not a barrier in principle', and in 1947 he published the first proposals for aberration correctors [2]. To overcome the technical barrier itself, it took most of the intervening 60 years, needing the development of fast computers and sensitive CCD detectors to diagnose and correct for the aberrations. Successful aberration correction came first with the scanning electron microscope [3] followed by the transmission electron microscope (TEM) [4–6] and the STEM [7,8].

These advances have given the STEM a much smaller brighter probe, allowing not only an improved spatial resolution, but also an improved signal to noise ratio, as a result of which the full advantages of the STEM have now been realized in practice. Multiple, simultaneous signals can readily be obtained to allow unprecedented insights into materials (for recent reviews, see [9–12]). These signals include high-angle annular dark-field (HAADF) or *Z*-contrast images, medium-angle annular dark-field (MAADF) for improved detection efficiency and strain-contrast imaging, bright-field phase-contrast imaging with improved efficiency and spectroscopic imaging for mapping of composition and, through the spectral fine structure, mapping of electronic structure such as orbital occupation.

Recently, annular bright-field imaging, originally proposed by Rose [13], has also been realized in practice, providing the sensitivity of a phase-contrast image with many of the desirable incoherent characteristics of a *Z*-contrast image [14–18]. It has also been possible to reduce the accelerating voltage while maintaining the atomic resolution, allowing beam-sensitive materials such as graphene and BN to be studied below their damage threshold. MAADF images of BN resolved and distinguished

individual atoms of B, C, N and O in monolayer BN [19] and electron energy loss spectra (EELS) found localized electronic states at the edges of graphene flakes [20].

In this review, we show the present state of the art for determining atomic positions and the electronic structure for correlation with properties of the material, and look towards future needs and possibilities.

Accurate measurement of atomic positions

One of the benefits of aberration correction in the TEM was the virtual elimination of the so-called image delocalization caused by the objective lens aberrations. With the exit wave function being transferred more faithfully to the image, delocalization became reduced to that caused by the propagation through the specimen, specifically, dynamical diffraction with its associated beam broadening. The situation is then similar to that seen in *Z*-contrast images, except that because the *Z*-contrast images favor the more localized states, one would still expect *Z*-contrast images to be more localized than phase-contrast images. The new ability to locate light atomic columns with phase contrast and to quantify positions and occupations to an unprecedented accuracy found many applications [21–27]. In the STEM, bright-field phase-contrast images had always been possible in principle through the use of a small axial collector aperture, equivalent, by reciprocity, to the illumination aperture in the TEM [28,29]. Before aberration correction, however, the collector aperture had to be very small for a good phase contrast, resulting in extremely noisy phase-contrast images. After aberration correction, it was possible to increase the collector aperture by an order of magnitude while still preserving a good contrast transfer, so that high-quality phase-contrast images became possible on the STEM for the first time [30,31]. Hence, simultaneous *Z*-contrast and phase-contrast images could routinely be recorded in the STEM: two complementary signals with pixel-to-pixel correlation.

While the TEM enjoys a parallel recording, the serial acquisition of STEM can cause problems with drift. This can be minimized with a good room design [32] and by developing highly stable columns [33–35] or mitigated by multiple rapid exposures and/or drift correction procedures [36,37], resulting in accuracies that are comparable for TEM and STEM. Figure 1 shows an illuminating example of the use of simultaneous *Z*-contrast and bright-field imaging to quantify atomic positions across a ferroelectric/metal interface [38]. The *Z*-contrast image allows the ferroelectric displacement and lattice parameter to be obtained directly from the cation positions, while the phase-contrast image shows the oxygen columns with high accuracy, allowing the octahedral rotations to be measured. It is seen that the metal electrode, which does not have significant octahedral rotations, severely constrains the octahedral rotations in $BiFeO_3$, which is the origin of the lattice expansion seen in the *Z*-contrast image, and also resulted in a dielectric anomaly detected by EELS. In this case, displacements and tilts were measured with respect to the local Bi sublattice, so that most of the drift was thereby subtracted, and only the *variation* in the drift across each unit cell affected the accuracy of the measurement.

Spectroscopic imaging of composition with the atomic resolution

While atomic-resolution spectroscopy was demonstrated in 1993 [39,40], the smaller, brighter probes resulting from aberration correction have inspired a recent upsurge in the use of EELS at atomic

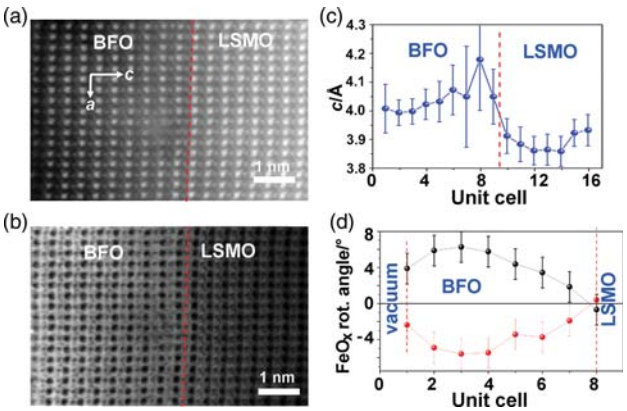

Fig. 1. Lattice parameters and octahedral tilts from STEM data: (a) HAADF STEM and (b) simultaneously acquired bright-field STEM images of the $SrTiO_3$/5 nm $La_{0.7}Sr_{0.3}MnO_3$/3.2 nm $BiFeO_3$ (BFO) ultrathin film; (c) profile of the *c* lattice parameter across the interface calculated from (a); (d) profile of FeO_x octahedral tilt angles in BFO calculated from (a) and (b). Note that lattice parameter enhancement at the interface in (c) coincides with a region of suppressed octahedral tilts in (d). Adapted from Ref. [38].

resolution (see [10] for a historical perspective). With third-order aberration correctors, line traces across individual unit cells revealed intriguing 'volcano' features, long predicted by theory, traced to the result of partial signal collection [41–45]. Nevertheless, identification of single impurity atoms within a crystal lattice became feasible [46] and the first two-dimensional atomic-resolution spectroscopic images were achieved under such conditions [47,48]. Two-dimensional maps could also be obtained even without aberration correction [49], but with the next generation of aberration correctors, and improved post-specimen optics, near 100% signal collection became possible for a wide range of elements [35]. Figure 2 shows an example of the spectroscopic imaging of GaAs, where enough signal is present in the Ga and As L edge signals (at more than 1 kV energy loss) to form good-quality atomic-resolution images.

EELS is also invaluable for distinguishing interface termination in cases where elements are difficult to distinguish based on *Z*-contrast alone. With third-order aberration correctors, this had to be done with line traces [50–52], but with fifth-order correctors, it is possible to see the termination directly in a two-dimensional image, bringing sensitivity to the presence of any defects in the stacking sequence. Figure 3 shows an example of a $YBa_2Cu_3O_{7-x}/La_{0.7}Ca_{0.3}MnO_3/YBa_2Cu_3O_{7-x}$ (YBCO/LCMO/YBCO) trilayer structure where both the top and bottom interfaces are clearly seen to be formed with the MnO_2 plane of the manganite (red) facing a BaO plane of the superconductor (blue).

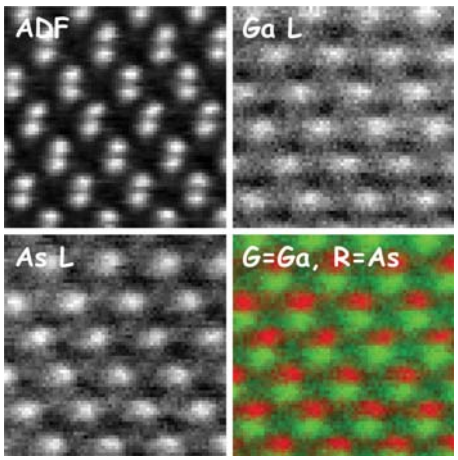

Fig. 2. Spectroscopic imaging of GaAs in the ⟨110⟩ projection comparing the ADF image with the Ga and As L spectroscopic images, obtained on a Nion UltraSTEM with a fifth-order aberration corrector operating at 100 kV. Images are 64 × 64 pixels, with collection time 0.02 s/pixel and a beam current of ~100 pA, after noise reduction by PCA [60].

Such images also have a sensitivity close to single-atom detection. Figure 4 shows an atomic-resolution compositional map of $Ca_xLa_{1-x}TiO_3/CaTiO_3$ bilayer doped with $x = 0.05$ La impurities. The La map shows an inhomogeneous distribution, and without any detailed image simulations a rough approximation of composition can be obtained just from the relative La/Ca intensity, as shown in Fig. 5 [53].

In reality, the sensitivity to La is depth-dependent due to the combined effects of channeling, which focuses electrons onto the columns, and scattering to high angles, which depletes the intensity on the column. These effects can be calculated and an example is shown in Fig. 6, where it is seen that the La intensity varies by about a factor of 2 with depth. Hence, the simple estimate is likely to be accurate to better than a factor of 2, offering immediate qualitative insights into the concentration distribution.

In this example, the La atoms are expected to be substituted for Ca, and viewing in the {100} orientation all the Ca columns are identical except for their La concentration, which allows for the simple interpretation. In Fig. 7, we show the more complicated case of $LaMnO_3$ (LMO) viewed along the [010]-direction, the {110}-direction in pseudocubic notation. This orientation facilitates resolution of the oxygen sublattice and directly reveals the octahedral rotations, allowing any changes to be tracked across interfaces and correlated with any associated changes in fine structure. However, in this projection there are now two types of O columns: pure O columns that show the octahedral rotations and LaO columns which are at the center of the octahedra and actually show a *minimum* in the O K edge intensity map. This behavior is also seen in the simulated image (Fig. 8). The reason of course is that the heavy LaO column leads to a rapid depletion in intensity with increasing specimen thickness, whereas the pure O columns show much slower depletion of intensity [45]. Figure 8 also shows simulations of the contribution of the two column types separately, showing the greatly

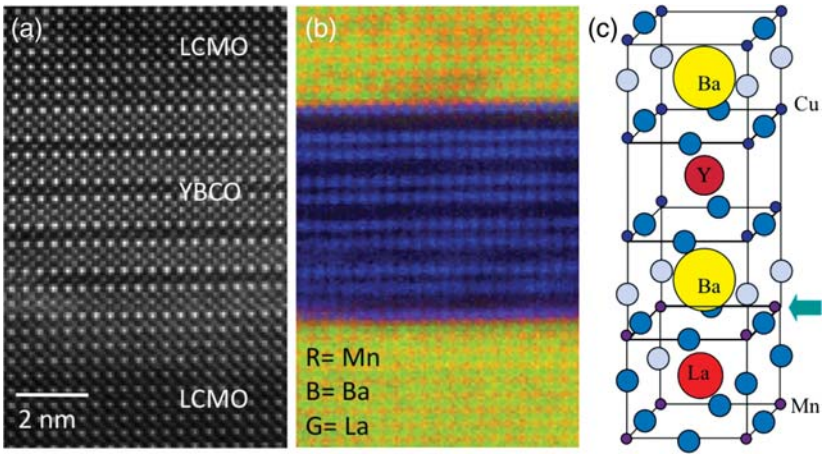

Fig. 3. (a) ADF signal collected simultaneously with a spectrum image in a LCMO/YBCO/LCMO trilayer. (b) False color image where three atomic-resolution elemental images have been overlayed: a Mn $L_{2,3}$ image in red, a Ba $M_{4,5}$ image in blue and a La $M_{4,5}$ image in green, for the same area as the *Z*-contrast in (a). The EELS data were acquired in the Nion UltraSTEM column and processed with PCA in order to remove random noise. (c) Sketch of the observed interface structure. An arrow marks the interface MnO_2 plane, which faces a BaO plane from the superconductor at both top and bottom interfaces.

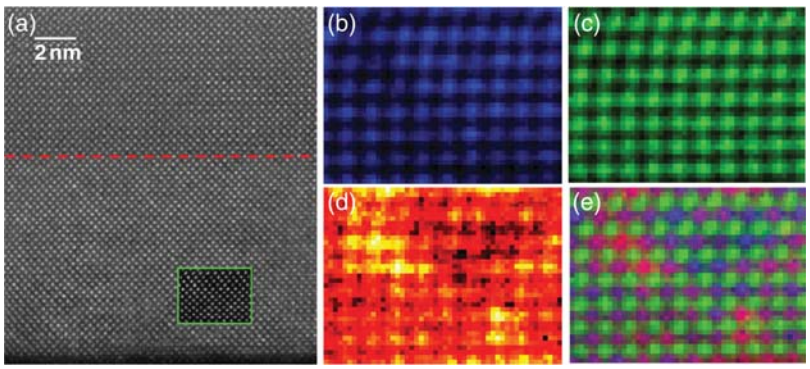

Fig. 4. (a) *Z*-contrast image of a $Ca_xLa_{1-x}TiO_3/CaTiO_3$ bilayer with $x = 0.05$ obtained at 100 kV in the fifth-order corrected Nion UltraSTEM. A red dotted line marks the position of the interface. The inset shows the region where a spectrum image was acquired, 50×37 pixels in size, with a current of ~100 pA and an exposure time of 0.1 s per pixel. The simultaneously acquired ADF signal is overlaid in the inset. Some spatial drift is observed. (b) Ca $L_{2,3}$ map, (c) Ti $L_{2,3}$ map and (d) La $M_{4,5}$ map, produced after noise removal using PCA and background subtraction using a power-law fit. The Ca and Ti maps were produced by integrating a 20 eV wide window, while for the La map, a 30 eV wide window was used. (e) RGB overlay of (b–d), with the La map shown in red, the Ti map in green and the Ca map in blue. Specimen courtesy of M. Biegalski and H. Christen from Oak Ridge National Laboratory.

reduced intensity of the O in the LaO column. Hence care needs to be taken in the direct interpretation of EELS images at atomic resolution. Electrons cannot be scattered simultaneously to the HAADF detector and to the spectrometer.

A spectacular example of the power of spectroscopic imaging is given in Fig. 9, showing images of a strained layer superlattice of thin layers of Y_2O_3-stabilized ZrO_2 (YSZ) between $SrTiO_3$ (STO) spacers. Such superlattices have recently been found to show up to eight orders of magnitude enhanced O ion conductivity near room temperature [54], creating intense interest for their potential to achieve high-efficiency fuel cells at low operating temperatures. The effect was found to scale with the number of interfaces and it was speculated that the origin of the effect lay in a combination of the large expansive lattice strain of the YSZ (7%) and the fact that the oxygen sublattices of the two materials are incompatible at the interface, the YSZ being a fluorite structure, and the STO a perovskite. EELS supported this interpretation, as the O K edge fine structure was somewhat washed out at the interface, indicative of disorder on the O sublattice, whereas no change was detected at Ti L edge, indicating that Ti remained in a 4+ state even at the

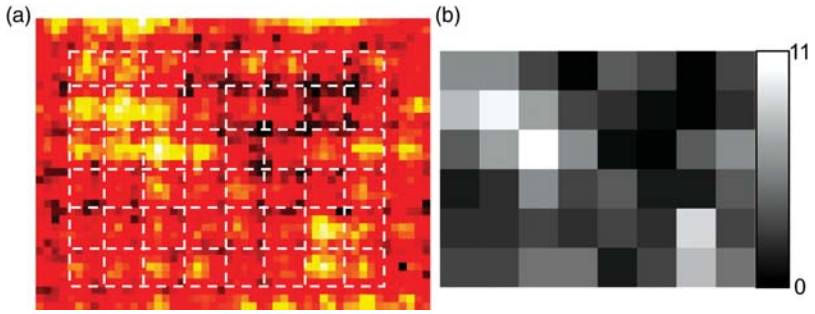

Fig. 5. (a) Grid marked on the La image from Fig. 6d. (b) Estimated number of isolated La atoms per column.

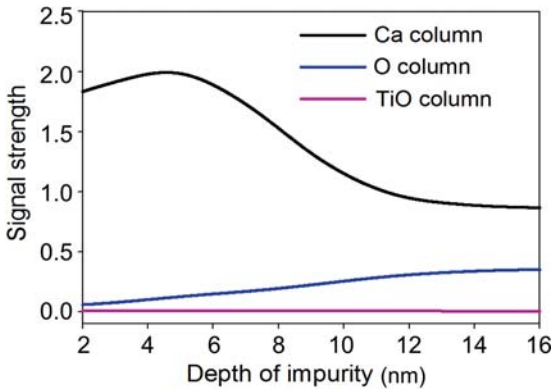

Fig. 6. Depth dependence of the La signal strength when the electron probe is sitting on the different Ca (black), O (blue) and Ti (pink) columns within the unit cell. Simulations done for optical parameters of the VG Microscopes HB501UX at 100 kV, as reported in Ref. [46].

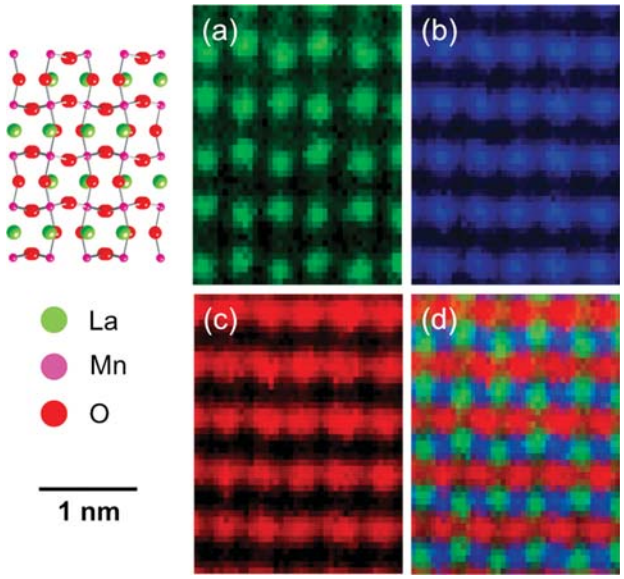

Fig. 7. Schematic showing the structure of $LaMnO_3$ along the [010] zone axis (pseudocubic ⟨110⟩ zone axis) with spectroscopic images using the O K, La $M_{4,5}$ and Mn $L_{2,3}$ edges in green, blue and red, together with a composite image (d). Octahedral rotations of the O sublattice are clearly visible in (a, d). Images are corrected for scan distortions. Reproduced from [77].

interface. Theoretical studies were subsequently undertaken, using density functional theory, and confirmed that the Ti preferred to keep a full octahedral coordination at the interface, explaining the EELS result. Finite temperature simulated annealing was carried out to investigate the stability of the O sublattice. It was found that straining ZrO_2 by 7% induced the O sublattice to take up a new phase at temperatures between 1000 and 2000 K, with O occupying a zigzag arrangement. At higher temperatures, the O sublattice became completely disordered. Performing the simulated annealing on a YSZ/STO superlattice, the disordered O sublattice appeared at only 360 K. Introducing O vacancies and calculating the mean square O displacements as a function of time, a six orders of magnitude-enhanced conductivity was predicted, confirming that the combination of expansive strain and interfacial mismatch of the O sublattice is indeed the origin of the colossal enhancement in ionic conductivity.

This theoretical result suggests, however, that the disordered O sublattice might be present even at room temperature and therefore that it may be possible to see the disorder directly in a core loss image. Figure 9b shows the *Z*-contrast image acquired simultaneously with the spectrum image [55]. Significant drift is present, but the cation sublattice is clearly visible. In the Ti core loss image (Fig. 9c) the YSZ layer is (largely) dark, indicating that the layer is predominantly YSZ. In the O K edge image (Fig. 9d), processed to remove noise using principal component analysis (PCA), the O sublattice is clearly visible in the STO, but not in the YSZ, confirming the expected disorder. The raw

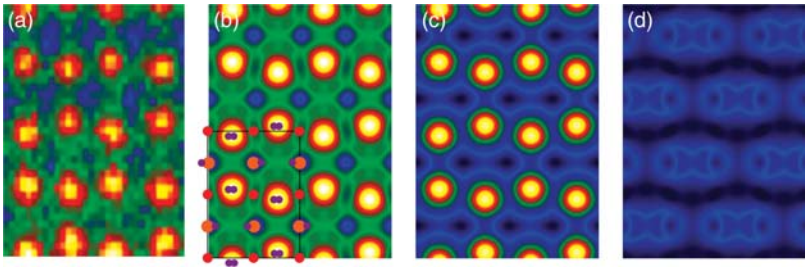

Fig. 8. Integrated oxygen K-shell EELS signal from $LaMnO_3$ in the [010] zone axis orientation (pseudocubic ⟨110⟩ axis). (a) Experimental image acquired on the Nion UltraSTEM operating at 60 kV. (b) Simulated image with projected structure inset. (c) Contribution to the total image from the isolated O columns. (d) Contribution to the total image from the O atoms on the La/O columns. Reproduced from Ref. [78].

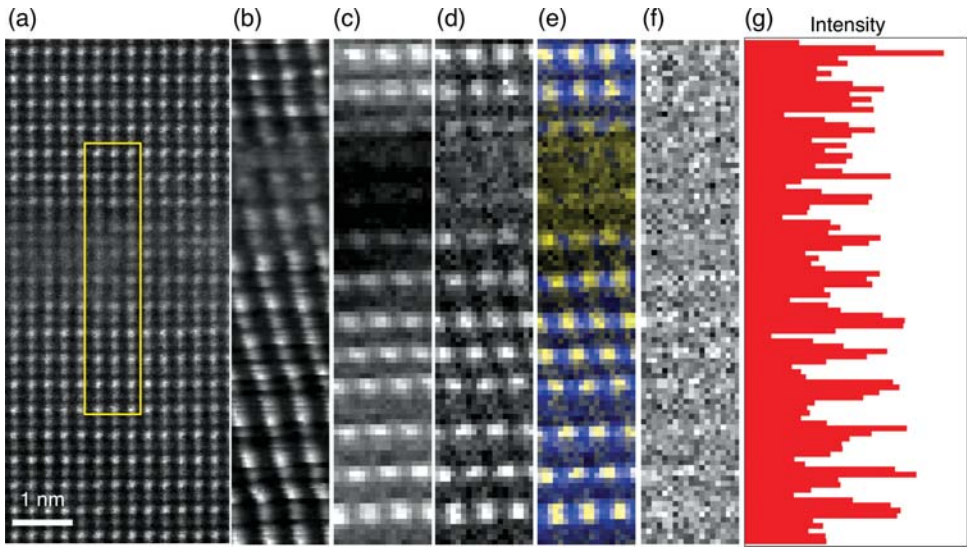

Fig. 9. (a) High-resolution ADF image of a section of coherent YSZ/STO multilayers viewed down the ⟨110⟩ STO axis. An ADF image recorded simultaneously with an SI taken in the area indicated by the yellow box is shown in (b). Integrated Ti L and O K edge intensity elemental maps extracted from the PCA processed SI are shown in (c) and (d) and as a composite map in (e) in which O intensity is shown in yellow and Ti intensity is shown in blue. An O elemental map extracted from the SI without PCA processing is shown in (f), and the integrated intensity of each row of pixels in the raw O map is shown in (g). The intensity is given in arbitrary units, with the background subtracted to improve the contrast. Reproduced from [55].

image data are shown in (Fig. 9f), in which the lattice structure in STO is just visible. A line trace across the superlattice shows that the intensity of the O signal is not changing across the superlattice, it is the lattice structure that just disappears. In contrast, the O sublattice could easily be resolved in the bulk YSZ [55].

Spectroscopic imaging of electronic structure with atomic resolution

Transition metal oxides show a very strong mixing of the Cu 3d bands and the O 2p bands near the Fermi level, so that both the transition metal L edge and the O K edge provide direct insights into the electronic structure, in particular, the hole concentration. Our first example is the high-temperature superconductor YBCO, in which the holes responsible for superconductivity have been established to reside on the CuO_2 planes through momentum-resolved EELS [56,57]. However, with spatially resolved EELS, this is immediately clear. Figure 10 shows an EELS line scan across several unit cells of YBCO, in which clear oscillations of the Cu L edge fine structure are seen. Figure 10b shows averaged spectra from the Cu chains (red) and planes (black), where the strong L3 line at ~931 eV shows a reduction by about a factor of 2 moving the beam from a CuO_2 plane to a CuO chain. This is similar to the observation by Nucker *et al.* [56] on changing

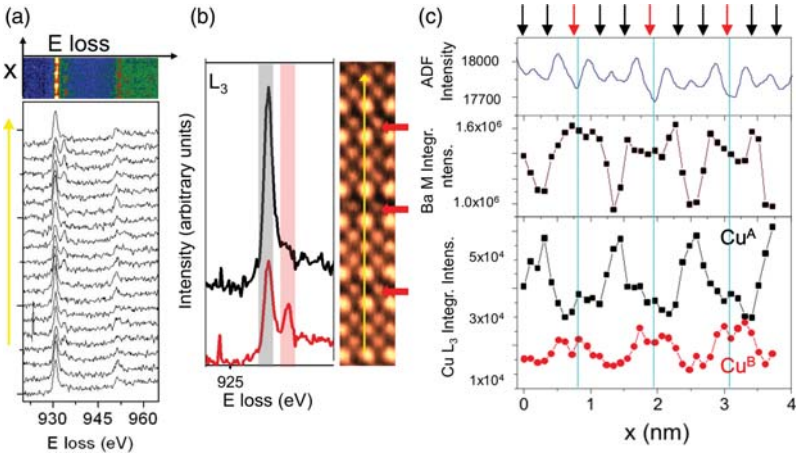

Fig. 10. (a) Cu $L_{2,3}$ spectra acquired as the electron beam is swept parallel to the YBCO *c*-axis. (b) Averaged L_3 line from the location of the CuO_2 planes (black) and the CuO chains (red). (c) Line trace marked in yellow in (b) showing the ADF signal, and the integrated intensity under the Ba $M_{4,5}$ edge. These allow the location of the CuO_2 planes and CuO chains along the scan. Red arrows mark the CuO chains, whereas black arrows the planes. The two lower panels show the integrated intensities under the first (in black) and second (in red) peaks of the split Cu L_3 line using windows such as those marked on (b). Data acquired in the aberration-corrected VG Microscopes HB501UX at 100 kV. The spectra have been averaged laterally to reduce noise.

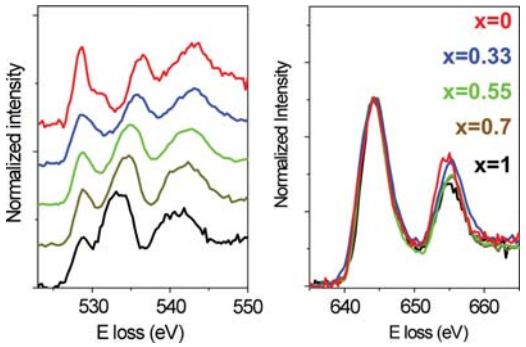

Fig. 11. O K (left) and Mn $L_{2,3}$ (right) edges for a set of $La_xCa_{1-x}MnO_3$ crystals oriented down the pseudocubic ⟨100⟩ axis for x values of 1 (black), 0.7 (brown), 0.55 (green), 0.33 (blue) and 0 (red). The O K edges have been displaced vertically for clarity, while the Mn L edges have been normalized and aligned for direct visual comparison. Adapted from Ref. [60].

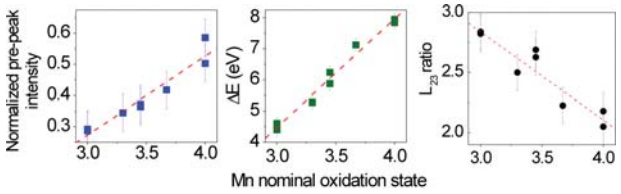

Fig. 12. O K edge normalized pre-peak intensity (left), peak separation, ΔE (center) and $L_{2,3}$ intensity ratio (right) versus nominal Mn oxidation state for the set of $La_xCa_{1-x}MnO_3$ crystals. Adapted from Ref. [60].

the momentum transfer from parallel to perpendicular to the *ab*- plane. In addition, a small higher energy peak is present predominantly on the chains, which appears to correlate with the ~934 eV peak characteristic of deoxygenated YBCO [56]. The presence of this peak may indicate some deoxygenation of the chain planes during spectrum acquisition; because of the additional vacant O sites in the chain planes than in the square planar CuO_2 planes, oxygen is expected to be more mobile in the chain planes. A line trace of these two peaks is shown in Fig. 10c, showing the correlation of the black peak to the planes and the red peak to the chains, which are distinguishable via the Ba M edge and ADF signals. The data were obtained with the third-order corrected VG Microscopes HB501UX, with a collection efficiency of only about 20%, and highlights the importance of being able to achieve 100% collection efficiency on the latest generation STEMs to minimize the electron dose required for good statistics.

The fine structure of the O K edge in YBCO also varies systematically with hole concentration [56–58], as it does in other transition metal oxides. Figure 11 shows the variation in O K and Mn $L_{2,3}$ edges in $La_xCa_{1-x}MnO_3$ (LCMO) as a function of x, with extracted linear dependencies on O K pre-peak to main peak ratio and separation, and the Mn $L_{2,3}$ intensity ratio shown in Fig. 12. These variations directly track Mn d-orbital occupation [59] and hence provide a convenient measure of local Mn valence, and have provided important insights into charge

transfer phenomena at complex oxide interfaces, explaining observed macroscopic superconducting and magnetic properties [50–52].

Such measurements can also be made at atomic resolution. Figure 13 compares theoretical and experimental spectra for the two inequivalent O sites in LMO, (apical O1 sites in black and equatorial O2 sites in blue). Experimental data are in good agreement with theory, except for a reduction in the magnitude of the changes due to the fact that dynamical diffraction somewhat mixes the signals from the two sites. The Mn valence is of course not changing, the changes reflect the different environments of the two O sites, and interpretation of fine structure at atomic resolution requires consideration of these effects [60]. A line trace of peak separation along the pseudocubic ⟨110⟩ direction of LMO is shown in Fig. 14.

Despite the apparent agreement between theory and experiment, these simulations imply a significant approximation. The density functional theory, even when the core hole interaction is included in a $Z+1$ calculation, implicitly assumes that the electron arrives at the atom in a plane wave state. This is a good assumption for the analagous case of X-ray absorption spectroscopy, but not for atomic-resolution EELS. In the aberration-corrected microscope, we have a coherent spherical wave forming the probe, and we also have dynamical diffraction in the case of zone axis crystals. While dynamical effects have been incorporated into EELS image simulations, these have mostly assumed the material to be a superposition of isolated atoms with no solid-state bonding, that is, no fine structure. Therefore, a number of investigations have been initiated to include both dynamical diffraction and solid-state bonding in a unified theoretical treatment which is expected to greatly improve the precision with which we can interpret EELS data in terms of the electronic structure of the material [61–63].

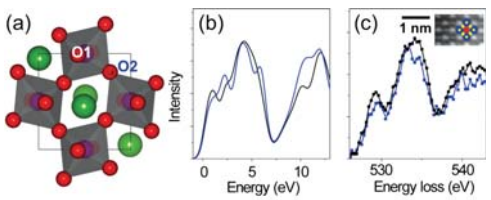

Fig. 13. (a) Sketch of the LMO structure, produced from the structural data reported by Rodriguez-Carvajal *et al.* [79]. (b) Simulated O K EELS for the O1 (black) and O2 (blue) species, adapted from Ref. [60]. (c) Experimental EELS from different positions (electron beam on top of a MnO column in black and on top of a La column in blue), extracted from a linescan along the pseudocubic ⟨110⟩ direction of LMO (data set in [60]). PCA was used to remove random noise. The LMO pseudocubic unit cell is shown on top of a *Z*-contrast image in the inset (La = red, Mn = blue, O = yellow).

Future directions

Now that the 'technical barrier' of spherical aberration has been overcome, where will microscopy venture next? Several possibilities present themselves. First, on a 'technical' front, it should be possible to autotune the aberrations from a single Ronchigram, which, being a signal that can be rapidly acquired, may allow autotuning during image or spectral acquisition, perhaps even from crystals [64,65]. Second, the challenge of microscopy in three dimensions will advance, possibly through the combination of depth sectioning [66–69] with tilt series reconstruction [70,71], perhaps with a confocal configuration [72,73]. Third, there are currently a number of efforts at aberration-corrected *in situ* microscopy, either with hot or cold stages [74] or in gas or liquid environments [75,76]. Fourth, the advantages of the STEM for multiple signal acquisition will surely be exploited further, correlating the imaging and analytical signals with those that reflect local functionality, for example, the use of electron-beam-induced current for mapping charge collection efficiency in solar cells, or cathodoluminescence for mapping light generation in materials for solid state lighting. With the increased current and reduced beam size now being available, it

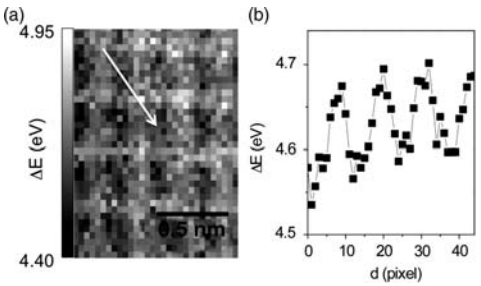

Fig. 14. (a) Peak separation map for the spectrum image giving rise to the O map in Fig. 11a, after PCA was applied to the raw data set for random noise removal. (b) Intensity profile for the image in (a), along the direction marked with a white arrow.

should be feasible to directly correlate atomic and electronic structure to electrical and optical properties.

Certainly, the barrier to atomic resolution has been well and truly overcome. For the next 60 years, indeed forever, atoms will be clearly seen in the electron microscope, and their electronic and optical properties will be correlated with local structure and bonding to further the quest for a true atomic-scale interpretation of macroscopic materials properties.

Funding

This work was funded by the US Department of Energy, Office of Basic Energy Sciences, Materials Sciences and Engineering Division.

Acknowledgements

The authors are grateful to A. Y. Borisevich, M. P. Oxley, T. J. Pennycook, S. T. Pantelides, J. Tao, W. Luo, M. Biegalski, H. M. Christen, H. J. Chang, M. D. Bieglaski, H. M. Christen, D. G. Mandrus, A. Rivera, F. Bruno, C. Leon, J. Santamaria, W. M. Sides and J. T. Luck for collaboration in this research.

References

1 Scherzer O (1936) Uber einige Fehler von Elektronenlinsen. *Z. Physik* **101**: 114–132.

2 Scherzer O (1947) Sparische und chromatische Korrektur von Electronen-Linsen. *Optik* **2**: 114–132.

3 Zach J and Haider M (1995) Aberration correction in a low voltage SEM by a multipole corrector. *Nucl. Instrum. Meth. A* **363**: 316–325.

4 Haider M, Rose H, Uhlemann S, Kabius B, and Urban K (1998) Towards 0.1 nm resolution with the first spherically corrected transmission electron microscope. *J. Electron Microsc.* **47**: 395–405.

5 Haider M, Rose H, Uhlemann S, Schwan E, Kabius B, and Urban K (1998) A spherical-aberration-corrected 200 kV transmission electron microscope. *Ultramicroscopy* **75**: 53–60.

6 Haider M, Uhlemann S, Schwan E, Rose H, Kabius B, and Urban K (1998) Electron microscopy image enhanced. *Nature* **392**: 768–769.

7 Krivanek O L, Dellby N, and Lupini A R (1999) Towards sub-angstrom electron beams. *Ultramicroscopy* **78**: 1–11.

8 Dellby N, Krivanek O L, Nellist P D, Batson P E, and Lupini A R (2001) Progress in aberration-corrected scanning transmission electron microscopy. *J. Electron Microsc.* **50**: 177–185.

9 Pennycook S J, Varela M, Chisholm M F, Borisevich A Y, Lupini A R, van Benthem K, Oxley M P, Luo W, McBride J R, Rosenthal S J, Oh S H, Sales D L, Molina S I, Sohlberg K, and Pantelides S T (2010) Scanning transmission electron microscopy of nanostructures. In: Narlikar A V and Fu Y Y (eds.), *The Oxford Handbook of Nanoscience and Nanotechnology*, pp. 205–248 (Oxford University Press, Oxford, UK).

10 Pennycook S J, Varela M, Lupini A R, Oxley M P, and Chisholm M F (2009) Atomic-resolution spectroscopic imaging: past, present and future. *J. Electron Microsc.* **58**: 87–97.

11 Pennycook S J, Chisholm M F, Lupini A R, Varela M, Borisevich A Y, Oxley M P, Luo W D, van Benthem K, Oh S H, Sales D L, Molina S I, Garcia-Barriocanal J, Leon C, Santamaria J, Rashkeev S N, and Pantelides S T (2009) Aberration-corrected scanning transmission electron microscopy: from atomic imaging and analysis to solving energy problems. *Phil. Trans. R. Soc. A* **367**: 3709–3733.

12 Pennycook S J, Chisholm M F, Lupini A R, Varela M, van Benthem K, Borisevich A Y, Oxley M P, Luo W, and Pantelides S T (2008) Materials applications of aberration-corrected STEM. In: Hawkes P W (ed.), *Aberration-corrected Electron Microscopy*, pp. 327–384 (Academic Press, Oxford, UK).

13 Rose H (1974) Phase-contrast in scanning-transmission electron-microscopy. *Optik* **39**: 416–436.

14 Findlay S D, Saito T, Shibata N, Sato Y, Matsuda J, Asano K, Akiba E, Hirayama T, and Ikuhara Y (2010) Direct imaging of hydrogen within a crystalline environment. *Appl. Phys. Express* **3**: 116603.

15 Findlay S D, Shibata N, Sawada H, Okunishi E, Kondo Y, and Ikuhara Y (2010) Dynamics of annular bright field imaging in scanning transmission electron microscopy. *Ultramicroscopy* **110**: 903–923.

16 Findlay S D, Shibata N, Sawada H, Okunishi E, Kondo Y, Yamamoto T, and Ikuhara Y (2009) Robust atomic resolution imaging of light elements using scanning transmission electron microscopy. *Appl. Phys. Lett.* **95**: 191913.

17 Okunishi E, Ishikawa I, Sawada H, Hosokawa F, Hori M, and Kondo Y (2009) Visualization of light elements at ultrahigh resolution by STEM annular bright field microscopy. *Microsc. Microanal.* **15**: 164–165.

18 Oshima Y, Sawada H, Hosokawa F, Okunishi E, Kaneyama T, Kondo Y, Niitaka S, Takagi H, Tanishiro Y, and Takayanagi K (2010) Direct imaging of lithium atoms in LiV_2O_4 by spherical aberration-corrected electron microscopy. *J. Electron Microsc* **59**: 457–461.

19 Krivanek O L, Chisholm M F, Nicolosi V, Pennycook T J, Corbin G J, Dellby N, Murfitt M F, Own C S, Szilagyi Z S, Oxley M P, Pantelides S T, and Pennycook S J (2010) Atom-by-atom structural and chemical analysis by annular dark-field electron microscopy. *Nature* **464**: 571–574.

20 Suenaga K and Koshino M (2010) Atom-by-atom spectroscopy at graphene edge. *Nature* **468**: 1088–1090.

21 Jia C L (2006) Atom vacancies at a screw dislocation core in $SrTiO_3$. *Phil. Mag. Lett.* **86**: 683–690.

22 Jia C L, Lentzen M, and Urban K (2003) Atomic-resolution imaging of oxygen in perovskite ceramics. *Science* **299**: 870–873.

23 Jia C L, Mi S B, Faley M, Poppe U, Schubert J, and Urban K (2009) Oxygen octahedron reconstruction in the $SrTiO_3/LaAlO_3$ heterointerfaces investigated using aberration-corrected ultrahigh-resolution transmission electron microscopy. *Phys. Rev. B* **79**: 081405.

24 Jia C L, Mi S B, Urban K, Vrejoiu I, Alexe M, and Hesse D (2009) Effect of a single dislocation in a heterostructure layer on the local polarization of a ferroelectric layer. *Phys. Rev. Lett.* **102**: 117601.

25 Jia C L, Thust A, and Urban K (2005) Atomic-scale analysis of the oxygen configuration at a $SrTiO_3$ dislocation core. *Phys. Rev. Lett.* **95**: 225506.

26 Jia C L and Urban K (2004) Atomic-resolution measurement of oxygen concentration in oxide materials. *Science* **303**: 2001–2004.

27 Urban K (2008) Studying atomic structures by aberration-corrected transmission electron microscopy. *Science* **321**: 506–510.

28 Cowley J M (1969) Image contrast in a transmission scanning electron microscope. *Appl. Phys. Lett.* **15**: 58–59.

29 Zeitler E and Thomson M G R (1970) Scanning transmission electron microscopy. *Optik* **31**: 258–280 and 359–366.

30 Pennycook S J, Chisholm M F, Varela M, Lupini A R, Borisevich A, Peng Y, van Benthem K, Shibata N, Dravid V P, Prabhumirashi P, Findlay S D, Oxley M P, Allen L J, Dellby N, Nellist P D, Szilagyi Z S,

and Krivanek O L (2004) Materials applications of aberration-corrected STEM. In: *2004 Focused Interest Group Pre-Congress Meeting 'Materials Research in an Aberration Free Environment')*.

31 Pennycook S J, Lupini A R, Varela M, Borisevich A Y, Peng Y, Oxley M P, van Benthem K, and Chisholm M F (2007) Scanning transmission electron microscopy for nanostructure characterization. In: Zhou W and Wang Z L (eds.), *Scanning Microscopy for Nanotechnology: Techniques and Applications*, pp. 152–191 (Springer, New York).

32 Muller D A and Grazul J (2001) Optimizing the environment for sub-0.2 nm scanning transmission electron microscopy. *J. Electron Microsc.* **50**: 219–226.

33 Müller H, Uhlemann S, Hartel P, and Haider M (2006) Advancing the hexapole C_s-corrector for the scanning transmission electron microscope. *Microsc. Microanal.* **12**: 442–455.

34 Kimoto K, Nakamura K, Aizawa S, Isakozawa S, and Matsui Y (2007) Development of dedicated STEM with high stability. *J. Electron Microsc.* **56**: 17–20.

35 Krivanek O L, Corbin G J, Dellby N, Elston B F, Keyse R J, Murfitt M F, Own C S, Szilagyi Z S, and Woodruff J W (2008) An electron microscope for the aberration-corrected era. *Ultramicroscopy* **108**: 179–195.

36 Saito M, Kimoto K, Nagai T, Fukushima S, Akahoshi D, Kuwahara H, Matsui Y, and Ishizuka K (2009) Local crystal structure analysis with 10-pm accuracy using scanning transmission electron microscopy. *J. Electron Microsc.* **58**: 131–136.

37 Kimoto K, Asaka T, Yu X, Nagai T, Matsui Y, and Ishizuka K (2010) Local crystal structure analysis with several picometer precision using scanning transmission electron microscopy. *Ultramicroscopy* **110**: 778–782.

38 Borisevich A Y, Chang H J, Huijben M, Oxley M P, Okamoto S, Niranjan M K, Burton J D, Tsymbal E Y, Chu Y H, Yu P, Ramesh R, Kalinin S V, and Pennycook S J (2010) Suppression of octahedral tilts and associated changes in electronic properties at epitaxial oxide heterostructure interfaces. *Phys. Rev. Lett.* **105**: 087204.

39 Batson P E (1993) Simultaneous STEM imaging and electron energy-loss spectroscopy with atomic-column sensitivity. *Nature* **366**: 727–728.

40 Browning N D, Chisholm M F, and Pennycook S J (1993) Atomic-resolution chemical-analysis using a scanning-transmission electron-microscope. *Nature* **366**: 143–146.

41 Rose H (1976) Image formation by inelastically scattered electrons in electron microscopy. *Optik* **45**: 139–158 and 187–208.

42 Allen L J, Findlay S D, Lupini A R, Oxley M P, and Pennycook S J (2003) Atomic-resolution electron energy loss spectroscopy imaging in aberration corrected scanning transmission electron microscopy. *Phys. Rev. Lett.* **91**: 105503.

43 Lupini A R and Pennycook S J (2003) Localization in elastic and inelastic scattering. *Ultramicroscopy* **96**: 313–322.

44 Oxley M P and Pennycook S J (2008) Image simulation for electron energy loss spectroscopy. *Micron* **39**: 676–684.

45 Oxley M P, Varela M, Pennycook T J, van Benthem K, Findlay S D, D'Alfonso A J, Allen L J, and Pennycook S J (2007) Interpreting atomic-resolution spectroscopic images. *Phys. Rev. B* **76**: 064303.

46 Varela M, Findlay S D, Lupini A R, Christen H M, Borisevich A Y, Dellby N, Krivanek O L, Nellist P D, Oxley M P, Allen L J, and Pennycook S J (2004) Spectroscopic imaging of single atoms within a bulk solid. *Phys. Rev. Lett.* **92**: 095502.

47 Okunishi E, Sawada H, Kondo Y, and Kersker M (2006) Atomic resolution elemental map of EELS with a C_s corrected STEM. *Microsc. Microanal.* **12**: 1150–1151.

48 Bosman M, Keast V J, Garcia-Munoz J L, D'Alfonso A J, Findlay S D, and Allen L J (2007) Two-dimensional mapping of chemical information at atomic resolution. *Phys. Rev. Lett.* **99**: Art. No. 086102.

49 Kimoto K, Asaka T, Nagai T, Saito M, Matsui Y, and Ishizuka K (2007) Element-selective imaging of atomic columns in a crystal using STEM and EELS. *Nature* **450**: 702–704.

50 Varela M, Lupini A R, Peña V, Sefrioui Z, Arslan I, Browning N D, Santamaria J, and Pennycook S J (2005). Direct measurement of charge transfer phenomena at ferromagnetic/superconducting oxide interfaces. http://arxiv.org/pdf/cond-mat/0508564v2.

51 Varela M, Lupini A R, Pennycook S J, Sefrioui Z, and Santamaria J (2003) Nanoscale analysis of $YBa_2Cu_3O_{7-x}/La_{0.67}Ca_{0.33}MnO_3$ interfaces. *Solid State Electron.* **47**: 2245–2248.

52 Varela M, Lupini A R, van Benthem K, Borisevich A, Chisholm M F, Shibata N, Abe E, and Pennycook S J (2005) Materials characterization in the aberration-corrected scanning transmission electron microscope. *Annu. Rev. Mater. Res.* **35**: 539–569.

53 Varela M, Gazquez J, Pennycook T J, Magen C, Oxley M P, and Pennycook S J (2011). Applications of aberration corrected scanning transmission electron microscopy and electron energy loss spectroscopy to complex oxide materials. In: Pennycook S J and Nellist P D (eds.), *Scanning Transmission Electron Microscopy* (Springer, New York).

54 Garcia-Barriocanal J, Rivera-Calzada A, Varela M, Sefrioui Z, Iborra E, Leon C, Pennycook S J, and Santamaria J (2008) Colossal ionic conductivity at interfaces of epitaxial ZrO_2:Y_2O_3/$SrTiO_3$ heterostructures. *Science* **321**: 676–680.

55 Pennycook T J, Oxley M P, Garcia-Barriocanal J, Bruno F Y, Leon C, Santamaria J, Pantelides S T, Varela M, and Pennycook S J (2011) Seeing oxygen disorder in YSZ/$SrTiO_3$ colossal ionic conductor heterostructures using EELS. *Eur. Phys. J. Appl. Phys.* in press.

56 Nucker N, Romberg H, Xi X X, Fink J, Gegenheimer B, and Zhao Z X (1989) Symmetry of holes in high-T_c superconductors. *Phys. Rev. B* **39**: 6619–6629.

57 Nucker N, Pellegrin E, Schweiss P, Fink J, Molodtsov S L, Simmons C T, Kaindl G, Frentrup W, Erb A, and Mullervogt G (1995) Site-specific and doping-dependent electronic-structure of $YBa_2Cu_3O_x$ probed by O 1s And Cu 2p X-ray-absorption spectroscopy. *Phys. Rev. B* **51**: 8529–8542.

58 Browning N, Yuan J, and Brown L (1992) Determination of the local oxygen stoichiometry in $YBa_2Cu_3O_\delta$ by electron-energy loss spectroscopy in the scanning-transmission electron-microscope. *Physica C* **202**: 12–18.

59 Luo W, Varela M, Tao J, Pennycook S J, and Pantelides S T (2009) Electronic and crystal-field effects in the fine structure of electron energy-loss spectra of manganites. *Phys. Rev. B* **79**: 052405.

60 Varela M, Oxley M P, Luo W, Tao J, Watanabe M, Lupini A R, Pantelides S T, and Pennycook S J (2009) Atomic-resolution imaging of oxidation states in manganites. *Phys. Rev. B* **79**: 085117.

61 Prange M, Oxley M P, Pennycook S J, and Pantelides S T (2011) Simulation of STEM-EELS including diffraction and solid-state effects I: mixed dynamic form factor beyond the dipole approximation. *Microsc. Microanal.* in press.

62 Pantelides S T, Pennycook T J, Luo W, Prange M, Lee H N, Oxley M P, Garcia-Barriocanal J, Bruno F Y, Leon C, Santamaria J, Chisholm M F, Varela M, and Pennycook S J (2011) Probing interfaces using a combination of scanning transmission electron microscopy and density-functional theory. *Microsc. Microanal.* in press.

63 Witte C, Findlay S D, Oxley M P, Rehr J J, and Allen L J (2009) Theory of dynamical scattering in near-edge electron energy loss spectroscopy. *Phys. Rev. B* **80**: 184108.

64 Lupini A R and Pennycook S J (2008) Rapid autotuning for crystalline specimens from an inline hologram. *J. Electron Microsc. (Tokyo)* **57**: 195–201.

65 Lupini A R, Wang P, Nellist P D, Kirkland A I, and Pennycook S J (2010) Aberration measurement using the Ronchigram contrast transfer function. *Ultramicroscopy* **110**: 891–898.

66 Borisevich A Y, Lupini A R, and Pennycook S J (2006) Depth sectioning with the aberration-corrected scanning transmission electron microscope. *Proc. Natl Acad. Sci. USA* **103**: 3044–3048.

67 Borisevich A Y, Lupini A R, Travaglini S, and Pennycook S J (2006) Depth sectioning of aligned crystals with the aberration-corrected scanning transmission electron microscope. *J. Electron Microsc.* **55**: 7–12.

68 van Benthem K, Lupini A R, Kim M, Baik H S, Doh S, Lee J H, Oxley M P, Findlay S D, Allen L J, Luck J T, and Pennycook S J (2005) Three-dimensional imaging of individual hafnium atoms inside a semiconductor device. *Appl. Phys. Lett.* **87**: 034104.

69 van Benthem K, Lupini A R, Oxley M P, Findlay S D, Allen L J, and Pennycook S J (2006) Three-dimensional ADF imaging of individual atoms by through-focal series scanning transmission electron microscopy. *Ultramicroscopy* **106**: 1062–1068.

70 Midgley P A, Weyland M, Thomas J M, and Johnson B F G (2001) *Z*-contrast tomography: a technique in three-dimensional nanostructural analysis based on Rutherford scattering. *Chem. Commun.* 907–908.

71 Weyland M, Midgley P A, and Thomas J M (2001) Electron tomography of nanoparticle catalysts on porous supports: a new technique based on Rutherford scattering. *J. Phys. Chem. B* **105**: 7882–7886.

72 Nellist P D, Behan G, Kirkland A I, and Hetherington C J D (2006) Confocal operation of a transmission electron microscope with two aberration correctors. *Appl. Phys. Lett.* **89**: 124105.

73 Nellist P D, Cosgriff E C, Behan G, and Kirkland A I (2008) Imaging modes for scanning confocal electron microscopy in a double aberration-corrected transmission electron microscope. *Microsc. Microanal.* **14**: 82–88.

74 Allard L F, Bigelow W C, Jose-Yacaman M, Nackashi D P, Damiano J, and Mick S E (2009) A new MEMS-based system for ultra-high-resolution imaging at elevated temperatures. *Microsc. Res. Tech.* **72**: 208–215.

75 Gai P L and Boyes E D (2009) Advances in atomic resolution in situ environmental transmission electron microscopy and 1 angstrom aberration corrected *in situ* electron microscopy. *Microsc. Res. Tech.* **72**: 153–164.

76 de Jonge N, Poirier-Demers N, Demers H, Peckys D B, and Drouin D (2010) Nanometer-resolution electron microscopy through micrometers-thick water layers. *Ultramicroscopy* **110**: 1114–1119.

77 Pennycook S, Borisevich A, Varela M, Lupini A, Chang H, Leonard D, Pennycook T, Oxley M, Idrobo J, Yurdakul H, Turan S, Yu P, Ramesh R, and Pantelides S (2010) Interface structure–property relations through aberration-corrected STEM. *Microsc. Microanal.* **16**: 1420–1421.

78 Oxley M, Chang H, Borisevich A, Varela M, and Pennycook S (2010) Imaging of light atoms in the presence of heavy atomic columns. *Microsc. Microanal.* **16**: 92–93.

79 Rodriguez-Carvajal J, Hennion M, Moussa F, Moudden A H, Pinsard L, and Revcolevschi A (1998) Neutron-diffraction study of the Jahn–Teller transition in stoichiometric $LaMnO_3$. *Phys. Rev. B* **57**: R3189.